

COSMIC Variance in Binary Population Synthesis

KATELYN BREIVIK,¹ SCOTT C. COUGHLIN,^{2,3} MICHAEL ZEVIN,^{2,4} CARL L. RODRIGUEZ,⁵ KYLE KREMER,^{2,4} CLAIRE S. YE,^{2,4} JEFF J. ANDREWS,^{2,4,6} MICHAEL KURKOWSKI,⁷ MATTHEW C. DIGMAN,⁸ SHANE L. LARSON,^{9,10} AND FREDERIC A. RASIO^{9,10}

¹Canadian Institute for Theoretical Astrophysics, University of Toronto, 60 St. George Street, Toronto, Ontario, M5S 1A7, Canada

²Center for Interdisciplinary Exploration and Research in Astrophysics (CIERA), Northwestern University,
 2145 Sheridan Road, Evanston, IL 60208, USA

³Physics and Astronomy, Cardiff University, Cardiff, CF10 2FH, UK

⁴Department of Physics and Astronomy, Northwestern University, 1800 Sherman Ave, Evanston, IL 60201, USA

⁵Harvard Institute for Theory and Computation, 60 Garden St, Cambridge, MA 02138, USA

⁶Niels Bohr Institute, University of Copenhagen, Blegdamsvej 17, 2100 Copenhagen, Denmark

⁷Department of Physics, University of Notre Dame, 225 Nieuwland Science Hall, Notre Dame, IN 46556, USA

⁸Center for Cosmology and AstroParticle Physics (CCAPP), Ohio State University, Columbus, OH 43210, USA

⁹Department of Physics & Astronomy, Northwestern University, Evanston, Illinois 60202, USA

¹⁰Center for Interdisciplinary Exploration & Research in Astrophysics (CIERA), Evanston, Illinois 60202, USA

(Revised September 1, 2022)

Submitted to ApJ

ABSTRACT

The most numerous sources for gravitational wave observatories are inspiraling and/or merging compact binaries. Simulations of large compact binary populations serve to both predict and inform observations of gravitational wave sources and their progenitors. Binary population synthesis (BPS) is a tool that balances physical modeling with simulation speed to produce large binary populations on timescales of \sim days. We present a new, openly developed, BPS suite: COSMIC which is designed to simulate compact binary populations and their progenitors. As a proof of concept, we simulate the Galactic population of compact binaries and their gravitational wave signal observable by the Laser Interferometer Space Antenna (*LISA*). We find that $\sim 10^8$ compact binaries reside in the Milky Way today, while $\sim 10^4$ of them may be resolvable by *LISA*.

Keywords: binaries: close – gravitational waves – methods: statistical

1. INTRODUCTION

Binary systems containing stellar remnants are the most prolific sources for both ground- and space-based gravitational wave (GW) observatories. The Laser Interferometer Gravitational Wave Observatory and Virgo (*LIGO/Virgo*) have detected the inspiral and merger of ten binary black holes (BBHs) and one binary neutron star (BNS; Abbott et al. (2018)). The Laser Interferometer Space Antenna (*LISA*) is expected to observe the population of $\sim 10^7$ binary stellar remnants, or compact binaries, in the Milky Way and its surrounding environ-

ment forming a confusion foreground of gravitational radiation in the millihertz region of the GW spectrum. Of these 10^7 binaries, tens of thousands are expected to be resolved above the foreground, offering a unique probe of the populations of stellar remnants in the local Universe (Nelemans et al. 2001; Korol et al. 2017; Lamberts et al. 2018, 2019).

Simulations of compact binary populations are useful tools that enable astrophysical interpretations of GW sources and their progenitors. BPS combines single star evolution with prescriptions for binary interactions to simulate binary populations from zero age main sequence to the stellar remnant phase. Generally, each BPS study seeks to determine which physical processes are most important in shaping observed catalog sources.

Corresponding author: Katelyn Breivik
 kbreivik@cita.utoronto.ca

To this end, in each study a single population and its detection catalog are simulated for a single model or a set of several models that canvass the available parameter space.

Several BPS codes are currently in use, each with their own simulation techniques and focuses. This type of simulation originated with the work of Whyte & Eggleton (1985) and has since been widely applied to the study of many different binary populations of interest. One approach is to modify a stellar evolution code previously developed for single stars to include the effects of binary evolution, as found in ev/STARS/TWIN (Pols et al. 1995; Nelson & Eggleton 2001), BINSTAR (Siess et al. 2013), MESA (Paxton et al. 2011, 2013, 2015, 2018, 2019), or BPASS (Eldridge & Stanway 2016; Stanway et al. 2016; Eldridge et al. 2017; Stanway & Eldridge 2018). Another approach is to generate large libraries of lookup tables for single stars and then use interpolation combined with simple binary evolution prescriptions, as done in SEVN (Spera et al. 2015; Spera & Mapelli 2017; Spera et al. 2019) or COMBINE (Kruckow et al. 2018).

The most widely applied technique is to use fitting formulae derived from single star evolution models, which vary as a function of stellar age, mass, and metallicity. For example Hurley et al. (2000) developed such a formalism based on the stellar evolution models of Pols et al. (1998). Different binary evolution prescriptions are applied to these fitting formulae to develop BPS codes, such as BSE (Hurley et al. 2002), SEBA (Portegies Zwart & Verbunt 1996; Nelemans et al. 2001; Toonen et al. 2012), the Brussels population number synthesis code (PNS) (De Donder & Vanbeveren 2004), STARTTRACK (Belczynski et al. 2002, 2008), BINARY_C (Izzard et al. 2004, 2006, 2009), COMPAS (Stevenson et al. 2017; Barrett et al. 2018), and MOBSE (Giacobbo et al. 2018; Giacobbo & Mapelli 2018). Given the wide variety of available software, studies like the POPCORN project, which compared the outputs of SEBA, STARTTRACK, BINARY_C, and the Brussels PNS code, are an invaluable resource to quantify theoretical uncertainties (Toonen et al. 2014). More recent population synthesis tools which use Markov-Chain Monte Carlo methods (`dart_board`; Andrews et al. 2018), Gaussian processes (Barrett et al. 2017; Taylor & Gerosa 2018), or Adaptive Importance Sampling (STROOPWAFEL; Broekgaarden et al. 2019) are also available to provide better statistical descriptions of binary populations.

Here we present COSMIC¹ (Compact Object Synthesis and Monte Carlo Investigation Code), a BPS code

that generates large binary populations which can be convolved with star formation history (SFH) and spatial distribution models to produce astrophysical realizations of binary populations. Simulated detection catalogs from these astrophysical realizations can then inform the range of possible compact binary populations detectable with both gravitational or electromagnetic observations. The ability to generate a statistical sample of binary populations is especially important when considering populations with low numbers. For example, the subset of mass transferring double white dwarfs (DWDs) with helium accretors observable by *LISA* and *Gaia* is expected to contain *dozens* of systems, which are a tiny subset of the tens of thousands of DWDs individually detectable by *LISA* (Kremer et al. 2017; Breivik et al. 2018).

The paper is organized as follows. In Sec. 2 we summarize the key features of COSMIC. We detail the additional binary evolution prescriptions that have been added to the version of BSE used in COSMIC in Sec. 3. In Sec. 4 we demonstrate the capabilities of COSMIC to produce a reference population of compact binaries observable by *LISA*. We finish with a discussion in Sec. 5.

2. OVERVIEW: COSMIC

One of the main features of COSMIC is its ability to determine *adaptively* the size of a simulated binary population such that it adequately describes the population's parameter distributions based on the user's need. Additionally, COSMIC is also able to simulate a population with a predetermined size. All data used to generate a population of binaries, including the parameters of stochastic processes like natal kicks for compact objects, as well as the properties of the population itself, are saved in the output of COSMIC. This allows a user to analyze the entire population as well as individual interesting systems to study in more detail, from the zero-age main sequence (ZAMS) all the way to compact object formation. In the subsections below, we outline several features in COSMIC using the Galactic population of compact binaries observable by *LISA* as an illustrative sample.

2.1. Fixed population

The main output from COSMIC is the fixed population, a collection of binary systems that contains enough binaries to capture the underlying shape of the population's parameter distribution functions resulting from a user-specified star SFH and binary evolution model. The fixed population can be convolved with more complex SFHs and scaled to a large number of astrophysical populations. These populations can then be synthetically “observed” and used to explore the variance in

¹ <https://cosmic-popsynth.github.io/>

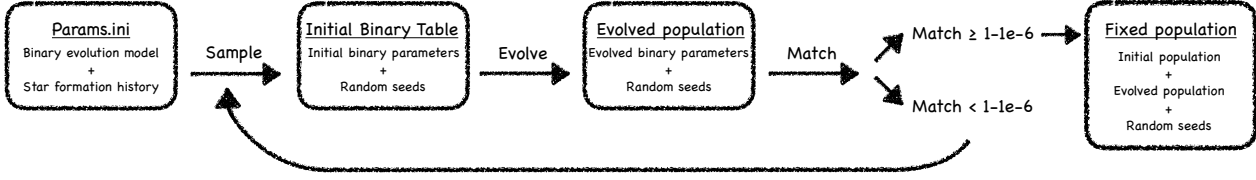


Figure 1. Schematic for the process COSMIC uses to generate a fixed population. Generally, the process moves from left to right. All quantities in the boxes are produced and available to the user, while all arrows represent modules within COSMIC that facilitate the evolution process. See also the list of steps outlined below in Section 2.

synthetic catalogs associated with the simulated binary population and binary evolution model.

The general process to simulate a fixed population is as follows:

1. Select a binary evolution model and SFH.
2. Generate an initial population based on user-selected models for the SFH and initial binary parameter distributions.
3. Evolve the initial population according to the user-specified SFH.
4. If on the first iteration, compare a subset containing half of the simulated population to the total population to determine how closely the binary parameter distributions match one another (we introduce a quantitative ‘match’ condition for making this assessment, described in Sec 2.1). If on the second or later iteration, compare the population from the previous iteration to the population containing both the current and previous iteration.
5. If the binary parameter distributions have converged, the population is called the ‘fixed population’ – a large enough sample to contain the essential statistical features of a fully evolved BPS model.
6. Scale the fixed population to astrophysical populations, weighted either by mass or by number, by sampling the fixed population with replacement.
7. Apply a synthetic observation pipeline to generate a set of synthetic catalogs from the astrophysical populations.

Figure 1 illustrates the structure and process COSMIC uses to generate the fixed population. The fixed population is simulated once for each combination of SFH and binary evolution model; thus a study with, for example, ten binary evolution models and one SFH will have ten associated fixed populations. Astrophysical populations can then be sampled from the fixed population and used to generate a statistical set of synthetic

catalogs for each model (i.e. a full study with ten binary evolution models and one SFH may contain *ten thousand* synthetic catalogs).

2.1.1. Initializing a population

The demonstration of COSMIC presented in this paper evolves binary populations using the binary stellar evolution code BSE, with several modifications including updated common envelope, wind, and kick prescriptions which are described further in Sec. 3. Regardless of binary evolution model, the fixed population is generated from an initial population of binaries sampled from distribution functions to assign each binary with an initial metallicity (Z), primary mass (m), mass ratio (q), orbital separation (a), eccentricity (e), and birth time (T_0) according to a given SFH. Since binary evolution codes generally evolve a single binary at a time, initial binary populations can be generated using several different star formation histories and distribution functions.

COSMIC is currently equipped to generate initial populations according to several binary parameter distributions. If the parameters are treated independently, initial masses may be sampled from a [Salpeter \(1955\)](#), [Kroupa et al. \(1993\)](#), or [Kroupa \(2001\)](#) initial mass function (IMF); mass ratios are uniformly sampled ([Mazeh et al. 1992](#); [Goldberg & Mazeh 1994](#)); orbital separations are sampled according to [Han \(1998\)](#); eccentricities may be sampled from a thermal distribution ([Heggie 1975](#)) or uniform distribution ([Geller et al. 2019](#)); binarity can be assumed to have user-specified fractions or the mass-dependent fraction of [van Haaften et al. \(2013\)](#). COSMIC is also able to generate initial binary samples following the [Moe & Di Stefano \(2017\)](#) multi-dimensional binary parameter distributions, which include mass and separation dependent binary fractions. For easy comparison to previous studies, we use independently distributed parameters with primary masses following the [Kroupa et al. \(1993\)](#) IMF, a thermal eccentricity distribution and a constant binary fraction of 0.5. For a study of the impact of multi-dimensional initial distributions on compact object populations see [de Mink & Belczynski \(2015\)](#) and [Klencki et al. \(2018\)](#).

The current version of COSMIC can generate populations according to very simple SFH prescriptions. For a more detailed study of the importance of SFH, see [Lamberts et al. \(2018\)](#). In many cases, it is useful to initially choose a single burst of star formation and later convolve the population with a SFH appropriate for the astrophysical population of interest.

2.1.2. Convergence of parameter distributions

There is no formulaic way to *a priori* predict the required number of binaries to be evolved for a fixed population, since each population depends on a different binary evolution model. The ideal number of simulated systems in a fixed population is such that the population adequately describes the final parameter distribution functions while not simulating so many systems as to be inefficient. To quantify this number, we apply a *match* criteria, based on matched filtering and template matching techniques, to histograms of binary parameter data from our simulated populations.

We use independently generated histograms for each binary parameter, with binwidths determined using Knuth's Rule ([Knuth 2006](#)) implemented in ASTROPY ([Astropy Collaboration et al. 2013](#)), to track the distribution of each parameter as successive populations are simulated and cumulatively added to the fixed population. Before each histogram is generated, we ensure that similar binwidths are used for each parameter as well as enforce the physical limits of the simulated systems (e.g. positive definite values for mass and orbital period and eccentricities between 0 and 1).

We define the *match* as

$$match = \frac{\sum_{k=1}^N P_{k,i} P_{k,i+1}}{\sqrt{\sum_{k=1}^N (P_{k,i} P_{k,i}) \sum_{k=1}^N (P_{k,i+1} P_{k,i+1})}}, \quad (1)$$

where $P_{k,i}$ denotes the probability for the k^{th} bin for the i^{th} iteration. The *match* is limited to values between 0 and 1 and tends to unity as the parameter distributions converge to a distinct shape. The *match* is specified by the user, and can be set to any value. For the study below, we set $match >= 1 - 10^{-6}$ as a fiducial choice, but caution that the results of each simulation should be carefully checked to confirm that the population does not contain artificial gaps due to low-number statistics.

2.2. Generating astrophysical population realizations

Once the fixed population satisfies the user-specified convergence criteria, an astrophysical population can be sampled and each binary in the astrophysical population

can be assigned a position and orientation. The number of sources in each astrophysical population can be calculated by normalizing the size of the fixed population by the ratio of the mass of the astrophysical population to the mass of stars formed to produce the fixed population:

$$N_{\text{astro}} = N_{\text{fixed}} \frac{M_{\text{astro,tot}}}{M_{\text{fixed,stars}}}, \quad (2)$$

or by the ratio of the number of stars in the astrophysical population to the total number of stars formed to produce the fixed population:

$$N_{\text{astro}} = N_{\text{fixed}} \frac{N_{\text{astro,tot}}}{N_{\text{fixed,stars}}}. \quad (3)$$

For each astrophysical realization, N_{astro} binaries are sampled with replacement from the fixed population. These sampled binaries can also be assigned a three dimensional position and an inclination (i), an argument of periapsis (ω), and a longitude of the ascending node (Ω).

COSMIC allows for several general Galactic position distributions. For the axisymmetric thin and thick disks, the radial and vertical distributions are assumed to be independent. We adopt Galactic position distributions and Galactic component masses from [McMillan \(2011\)](#) as a fiducial model. However, sources may be distributed according to exponential distributions in the radial and vertical directions with any scale height, as well as in spherically symmetric distributions.

Following [McMillan \(2011\)](#), we assume the mass in the thin and thick disks to be $4.32 \times 10^{10} M_{\odot}$ and $1.44 \times 10^{10} M_{\odot}$ respectively, while we assume the mass of the bulge to be $8.9 \times 10^9 M_{\odot}$. Finally, we emphasize that while COSMIC has utility functions implemented to distribute binaries in the Milky Way, the spatial distributions are independent of the binary evolution prescriptions. Thus multiple spatial distributions can be assumed for a single fixed population and more sophisticated spatial distribution models can be integrated into future releases of COSMIC.

3. UPDATES TO BSE

COSMIC uses a modified version of BSE to evolve binaries from zero-age main sequence through to compact object formation. The modified version of BSE currently used by COSMIC contains several upgrades which are briefly described below. The version containing these upgrades is fixed as v3.1.0 [Breivik et al. \(2019\)](#). All future modifications will be openly developed in the COSMIC Github repository².

² <https://github.com/COSMIC-PopSynth/COSMIC>

3.1. Winds

Mass loss through stellar winds plays an important role in compact object formation because this determines the mass of the star just before it undergoes a supernova (SN) explosion (e.g., Mapelli et al. 2009; Belczynski et al. 2010; Fryer et al. 2012; Giacobbo et al. 2018). In recent years, models of stellar winds have been revised to reflect updates in our understanding of various relevant physical processes. We have amended the original BSE stellar wind prescriptions with several of these prescriptions, summarized below.

Recent work has shown that line-driven winds exhibit strong dependence upon metallicity both on the main sequence (MS) and post-MS (e.g., Vink et al. 2001; Meynet & Maeder 2005; Gräfener & Hamann 2008; Vink et al. 2011). We have updated the original BSE to include metallicity-dependent winds for O and B stars as well as for Wolf-Rayet stars. The winds for O and B stars are treated according to the prescription of Vink et al. (2001), which considers stars with temperatures $12,500 \text{ K} < T_{\text{eff}} < 22,500 \text{ K}$ and $27,500 \text{ K} < T_{\text{eff}} < 50,000 \text{ K}$ separately. As in Rodriguez et al. (2016), we adopt the methods of Dominik et al. (2013) where the high and low temperature prescriptions are extended to $T_{\text{eff}} = 25,000 \text{ K}$. Wolf-Rayet stars are treated according to Vink & de Koter (2005).

Additionally, recent models suggest that as stars approach the limit imposed by the electron-scattering Eddington factor, $\Gamma_e = \chi_e L / (4\pi c GM)$ where χ_e is electron scattering opacity, winds may become insensitive to metallicity (e.g., Gräfener & Hamann 2008; Vink et al. 2011; Chen et al. 2015). Thus, we include Eddington-limited winds using the prescriptions described in Gräfener & Hamann (2008); Giacobbo et al. (2018).

If the primary star loses mass through a stellar wind, the secondary may accrete some of the ejected material as it orbits through it. The accretion rate onto the secondary can be estimated according to a Bondi-Hoyle type mechanism (Bondi & Hoyle 1944), which is sensitive to the velocity of the wind lost from the primary, $v_w^2 = 2\beta_w GM/R$, where β_w is a constant depending on stellar type (see equation 9 of Hurley et al. 2002). We have implemented β_w values from Belczynski et al. (2008), but assume as a default that $\beta_w = 0.125$ following Hurley et al. (2000).

3.2. Mass transfer stability and common envelope

The stability of Roche-lobe overflow mass transfer is determined through the same process as in Hurley et al. (2002), using critical mass ratios determined from radius-mass exponents (Webbink 1985). However, we

have added new models that are consistent with Claeys et al. (2014) and we have modified the critical mass ratios of MS/He-MS stars and binaries with degenerate accretors based on de Mink et al. (2007). For the models which are consistent with Claeys et al. (2014), we also adopt the Roche-lobe overflow mass transfer rates in Eq. (10) in the case of stable mass transfer. Finally, we note that COSMIC allows for user-specified critical mass ratios based on evolutionary stages to allow easy implementation with future models as they arise.

We employ the standard $\alpha\lambda$ model for common envelope (CE) evolution as done in Hurley et al. (2002). In this case, systems which undergo unstable mass transfer enter into a CE which can be expelled by the injection of orbital energy from the binary. In this formalism, λ is a factor which determines the binding energy of the envelope to its stellar core, while α is the efficiency factor for injecting orbital energy into the envelope. The current implementation of BSE defaults to a variable λ which depends on the evolutionary state of the star following the description in the Appendix of Claeys et al. (2014). However, constant λ is also allowed.

As a fiducial CE model, we use the variable binding energy parameter in conjunction with a constant CE efficiency parameter $\alpha = 1.0$ following previous results (e.g., Nelemans et al. 2001; Dominik et al. 2012). However, we note that previous studies of post-CE binaries point to an efficiency as low as $\alpha = 0.2$ (Zorotovic et al. 2010; Toonen & Nelemans 2013; Camacho et al. 2014). On the other hand, detailed modeling of the CE phase for DNS progenitors suggests CE efficiencies may be as high as $\alpha \approx 5$ (Fragos et al. 2019), which may also reduce the tension between rate predictions from CE channels (e.g., Mapelli & Giacobbo 2018) and the empirical DNS merger rate derived from *LIGO/Virgo* (Abbott et al. 2017).

We also include an option for a “pessimistic CE” scenario, in which unstable mass transfer from a donor star without a well-developed core-envelope structure is always assumed to lead to a merger (Belczynski et al. 2008). When this option is set, we also assume mergers to occur when unstable mass transfer is triggered from donor stars without a clear entropy jump at the core-envelope boundary (Ivanova & Taam 2004), which includes stars in the Hertzsprung Gap.

Mass transfer involving an evolved He-star donor and a compact object is a critical phase of binary evolution for forming hardened compact binaries that can merge within a Hubble time as GW sources. For progenitors of DNS, detailed modeling of this phase finds that mass transfer typically proceeds stably (Ivanova et al. 2003; Tauris et al. 2013, 2015) and does not lead to the onset of

a CE. Stable mass transfer is also corroborated by studies that compare population modeling to the properties of Galactic DNS (Vigna-Gómez et al. 2018). Post-mass-transfer separations are typically wider if this phase is modeled stably versus unstably. We allow for the stable mass-transfer evolution of He-star donors with compact object companions to be approximated using the fitting formulae in Tauris et al. (2015), which can fit for either the post-mass-transfer separation and remaining He-star envelope mass, or just the post-mass-transfer separation.

One important change implemented in COSMIC is the treatment of supernovae that directly follow a CE phase. By default, if a supernova immediately follows a CE (which typically occurs for evolved He-star donors), BSE determines the post-SN barycentric velocity, orbital properties, and survival using the *post-CE* orbital separation and *pre-CE* stellar mass. Therefore, the mass-loss in the supernova includes the mass of the donor-star envelope that formed the CE — a self-inconsistent treatment since the ejection of this envelope is used to determine the hardening during the CE phase. This inconsistency leads to artificially amplified mass-loss kicks during the supernova, which is particularly apparent in extremely tight binaries. Therefore, by default, we use the post-CE separation and post-CE mass (which does not include the mass of the envelope) when determining the impact of the subsequent supernova. The impact of this change, particularly on DNS population properties, is explained in more detail in Zevin et al. (2019).

3.3. Supernova explosion mechanisms and natal kicks

3.3.1. Standard Core-collapse Supernovae

Two new prescriptions for the supernova mechanism have been added to following Fryer et al. (2012), which account for material falling back onto the compact objects formed in core-collapse SNe, which are both convection-enhanced and neutrino driven. The two cases are delineated by the time between core bounce and explosion, with a ‘rapid’ explosion which only allows for explosions that occur within 250 ms and a ‘delayed’ explosion, which allows for longer timescales to explosion. The main difference in these two prescriptions is the presence of a mass gap between neutron stars and black holes which is produced in the rapid case but not present in the delayed case.

The inclusion of fallback onto compact objects reduces natal kick magnitudes due to the fraction of ejected mass during the supernova that falls back onto the compact object. As in the original version of BSE, natal kick magnitudes for standard iron core-collapse supernovae are drawn from a Maxwellian distribution with a disper-

sion of 265 km s^{-1} , consistent with the proper motions observed for isolated pulsars (Hobbs et al. 2005). The natal kick is then reduced by a factor of $1 - f_{\text{fb}}$, where f_{fb} is the fraction of the ejected supernova mass that will fall back onto the newly formed proto-compact object (see Eqs. (16) and (19) in Fryer et al. 2012). This efficiently damps the natal kicks for heavy ($M \gtrsim 30M_{\odot}$) black holes whose progenitors have CO core masses of $M_{\text{CO}} \geq 11M_{\odot}$. We also include options to allow for no natal kick, full natal kicks (with no reduction due to fallback), and “proportional” kicks that have black hole kicks scaled down by a factor of $m_{\text{BH}}/m_{\text{NS}}$, where m_{NS} is the maximum mass of a neutron star (assumed to be $2.5M_{\odot}$). An option is also included to scale down the natal kicks for all black holes by a constant factor, in addition to what fallback prescription is set.

By default, the natal kick is assumed to impact the proto-compact object in a direction that is isotropically sampled. However, correlations between the proper motions of pulsars and their spin axis suggest that the kick may be preferentially directed along the spin axis of a newly-formed compact object (Wang et al. 2006; Ng & Romani 2007; Kaplan et al. 2008). We therefore allow for the kick direction to be constrained within a specified opening angle around the poles of the proto-compact object. Alternatively, the natal kick magnitudes and directions for a binary can be input directly when evolving a binary.

3.3.2. Electron-capture Supernovae

A number of analyses have argued that for stars with main sequence masses in the range $\sim 8 - 11M_{\odot}$, the expected fate is a so-called electron-capture SN (ECSN; e.g., Miyaji et al. 1980; Nomoto 1984, 1987; Podsiadlowski et al. 2004; Ivanova et al. 2008). In this scenario, stars develop helium cores in the range of masses $\sim 1.5 - 2.5M_{\odot}$ and never develop an iron core. In this case, collapse is triggered by electron captures onto ^{24}Mg and ^{20}Ne which lead to a sudden drop of electron pressure support in the stellar core. The collapse occurs when the mass of the stellar core is $> 1.38M_{\odot}$ (Miyaji et al. 1980; Nomoto 1984, 1987; Ivanova et al. 2008).

The specific range of helium core masses expected to give rise to ECSNe is uncertain and several values have been proposed in the literature. In Hurley et al. (2002), the range $1.6 - 2.25M_{\odot}$ was implemented. Podsiadlowski et al. (2004) argued that a broader range of $1.4 - 2.5M_{\odot}$ is more realistic. Belczynski et al. (2008) implemented the relatively narrow range of $1.85 - 2.25M_{\odot}$, while Andrews et al. (2015) argue that a range of $2 - 2.5M_{\odot}$ is required to reproduce the distribution of DNSs in the Milky Way field. Here

we have updated the original BSE prescription to allow the lower and upper limits for the helium core mass range leading to ECSN to be specified directly.

In the case of an ECSN, the SN is expected to occur through a prompt (fast) explosion rather than a delayed neutrino-driven explosion; thus various analyses have argued that ECSNe likely lead to smaller NS natal kicks relative to core-collapse SNe (e.g., Podsiadlowski et al. 2004; Ivanova et al. 2008). By default, we assume kicks resulting from ECSN are drawn from a Maxwellian with dispersion velocity $\sigma_{\text{ECSN}} = 20 \text{ km/s}$, but include this as a variable to be specified directly by the user.

ECSNe may also occur through accretion-induced collapse (AIC) or merger-induced collapsed (MIC). Simple prescriptions are implemented for AIC and MIC in BSE (Hurley et al. 2002). For an ONeMg WD, if it is accreting CO or ONe material from its companion in a binary during RLOF, it will undergo AIC (Nomoto & Kondo 1991; Saio & Nomoto 2004) when its mass is larger than the ECSN critical mass. Furthermore, a merger/collision between two CO or ONe WDs leads to a MIC if the mass of the merger/collision product is larger than the ECSN critical mass. Both paths can lead to NS remnants if the mass of the final product is smaller than the maximum NS mass set by BSE.

3.3.3. Ultra-stripped Supernovae

For close binaries containing a BH or NS and a Roche-lobe filling helium star companion, the helium star may be sufficiently stripped of material such that a naked $\sim 1.5 M_{\odot}$ core remains (Tauris et al. 2013, 2015). The ensuing explosion of these ultra-stripped stars may lead to ejected mass $\lesssim 0.1 M_{\odot}$, which may yield natal kick velocities far below those expected for standard core-collapse SNe. Thus, it may be appropriate to draw kicks from a Maxwellian with dispersion width, σ , smaller than that of the standard Hobbs et al. (2005) distribution ($\sigma = 265 \text{ km s}^{-1}$). Here, whenever a helium star undergoes a CE phase with a compact companion such that a naked helium star forms, we implement the capability of assigning to these objects a smaller natal kick upon collapse and explosion as an ultra-stripped SNe.

3.3.4. Pair-instability and Pulsational Pair-Instability Supernovae

In the cores of post-carbon burning stars with sufficiently massive helium cores of $\gtrsim 30 M_{\odot}$, photons will readily convert into electron-positron pairs and diminish the pressure support of the core. This will cause the core to rapidly contract and the temperature to increase, allowing for the ignition of carbon, oxygen, or silicon (e.g. Woosley & Heger 2015). For helium-core masses of $\approx 30 - 64 M_{\odot}$, this spontaneous burning leads

to mass ejections, known as pulsational pair instabilities (PPIs, Woosley 2017). These will proceed until the instability is avoided. If the helium-core mass is in the range $\approx 64 - 133 M_{\odot}$, the instability exceeds the binding energy of the star and the star is completely destroyed — a pair instability supernova (PISN, Woosley 2017).

As our default, we adopt the prescription from Belczynski et al. (2016), which sets the maximum mass of the helium core below which the star is not destroyed by PISN to $45 M_{\odot}$ (resulting in a remnant black hole mass of $40.5 M_{\odot}$, assuming 10% of the mass is lost in the conversion from baryonic to gravitational mass). Helium core masses between $45 - 135 M_{\odot}$ lead to the destruction of the star through a PISN, and therefore no remnant formation. We allow for the limiting helium-core mass beyond which a PISN occurs to be set manually to different values.

Alternatively, multiple other prescriptions for determining the (P)PISN mass range and resultant remnant mass are available in COSMIC:

1. Prescription from Spera & Mapelli (2017) (see Appendix B), which is derived from fitting the masses of the compact remnants as a function of the final Helium mass fraction and final Helium core mass from the simulations in Woosley (2017).
2. Fit to the grid of simulations from Marchant et al. (2019) (see Table 1), which demonstrate a turnover in the relation between pre-supernova helium core mass and final mass. Similar to Stevenson et al. (2019), we use a 9th-order polynomial fit to map CO core masses between $31.99 \leq M_{\text{He}}/M_{\odot} \leq 61.10$ to black hole masses:

$$M_{\text{BH}} = \sum_{l=0}^7 c_l \left(\frac{M_{\text{He}}}{M_{\odot}} \right)^l, \quad (4)$$

where the coefficients are $c_0 = -6.29429263 \times 10^5$, $c_1 = 1.15957797 \times 10^5$, $c_2 = -9.28332577 \times 10^3$, $c_3 = 4.21856189 \times 10^2$, $c_4 = -1.19019565 \times 10^1$, $c_5 = 2.13499267 \times 10^{-1}$, $c_6 = -2.37814255 \times 10^{-3}$, $c_7 = 1.50408118 \times 10^{-5}$, and $c_8 = -4.13587235 \times 10^{-8}$.³ The PISN gap, which leaves behind no remnant, is $54.48 < M_{\text{CO}}/M_{\odot} < 113.29$.

3. Fit to the grid of simulations from Woosley (2019) (see Table 5), which agree reasonably well with those from Marchant et al. (2019) except that

³ We use different coefficients than in Stevenson et al. (2019) since the coefficients presented in this paper were found to be a poor match to the data from Marchant et al. (2019).

Woosley (2019) find slightly lower helium core masses undergo PPISN. We again fit a use a 9th-order polynomial fit, mapping CO core masses between $29.53 \leq M_{\text{He}}/\text{M}_{\odot} \leq 60.12$ to black hole masses, with coefficients $c_0 = -3.14610870 \times 10^5$, $c_1 = 6.13699616 \times 10^4$, $c_2 = -5.19249710 \times 10^3$, $c_3 = 2.48914888 \times 10^2$, $c_4 = -7.39487537$, $c_5 = 1.39439936 \times 10^{-1}$, $c_6 = -1.63012111 \times 10^{-3}$, $c_7 = 1.08052344 \times 10^{-5}$, and $c_8 = -3.11019088 \times 10^{-8}$. The PISN gap, which leaves behind no remnant, is $60.12 < M_{\text{CO}}/\text{M}_{\odot} < 113.29$.

3.4. Black Hole Spins

We have added additional prescriptions for the spins of newly-formed BHs from collapsing massive stars. Due to the uncertain values associated with BH natal spins, we allow the spins of all BHs to be set to a specific Kerr value (specified by the user) or drawn from a uniform distribution whose bounds are also user specified. In addition, we have included the prescriptions for BH spin based on the pre-collapse CO core mass of the progenitor from Belczynski et al. (2017), which result in high spins for low-mass BHs ($\lesssim 30\text{M}_{\odot}$, depending on metallicity) and low spins for high-mass BHs.

The latter prescription, based on stellar models computed by the GENEVA stellar evolution code (Eggenberger et al. 2008), assumes that angular momentum is transported in massive stars via meridional currents, and is not efficient enough to spin down the core prior to collapse. This is in contrast to newer work (e.g., Fuller & Ma 2019) suggesting that the Taylor-Spruit magnetic dynamo may allow for extremely efficient angular momentum transport through the envelopes of massive stars, producing BHs with dimensionless Kerr spin parameters $a/M \sim 0.01$. We do not include the latter prescription in COSMIC, nor do we allow for the BH spin to be increased by accretion or mergers. These effects will be added in a future release.

3.5. Pulsar Formation and Evolution

We have updated BSE to implement the NS magnetic field and spin period evolution following Kiel et al. (2008) and Ye et al. (2019). All NSs are born with magnetic fields and spin periods that match the observed young pulsars (Manchester et al. 2005); their initial magnetic fields and spin periods are randomly drawn in the range of $10^{11.5} - 10^{13.8}$ G, and 30 – 1000 ms, respectively.

For single NSs or NSs in detached binaries, we assume magnetic dipole radiation for the spin period evolution. The spin-down rate is calculated by

$$\dot{P} = K \frac{B^2}{P}, \quad (5)$$

where P is the spin period, B is the surface magnetic field and $K = 9.87 \times 10^{-48}$ yr/G². We also assume that the magnetic fields follow exponential decays in a timescale of $\tau = 3$ Gyr (Kiel et al. 2008),

$$B = B_0 \exp\left(\frac{-T}{\tau}\right), \quad (6)$$

where B_0 is the initial magnetic field, and T is the age of the NSs.

On the other hand, binary evolution will affect the NS magnetic fields and spin periods. For NSs in non-detached binaries, their magnetic fields can change significantly during mass accretion on short time scales. We assume “magnetic field burying” (e.g., Bhattacharya & van den Heuvel 1991; Rappaport et al. 1995; Kiel et al. 2008; Tauris et al. 2012) for the magnetic field decay during mass accretion

$$B = \frac{B_0}{1 + \frac{\Delta M}{10^{-6} M_{\odot}}} \exp\left(-\frac{T - t_{\text{acc}}}{\tau}\right). \quad (7)$$

ΔM is the mass accreted and t_{acc} is the accretion duration. These NSs are spun up according to the amount of angular momentum transferred (Hurley et al. 2002, equation (54)).

Furthermore, when a NS merges with another star (e.g., main-sequence star, giant, or WD) and the final product is a NS, the magnetic field and spin period of this NS are reset by drawing a new magnetic field and spin period from the same initial ranges. If a millisecond pulsar (MSP) is involved in the collision or merger, however, the newly-formed NSs are assigned different ranges of initial magnetic fields and spin periods to match those of MSPs, and the newborn NSs will remain MSPs. In this case, the magnetic fields and spin periods are randomly drawn from ranges $10^8 - 10^{8.8}$ G and 3 – 20 ms, respectively.

In addition, we assume a lower limit of 5×10^7 G for the NS magnetic field (Kiel et al. 2008). No lower limit is assumed for the spin periods.

3.6. Stellar Mergers

When two stellar cores spiral in toward one another, the outcome of the subsequent merger depends upon the internal structures (i.e., density profiles) of the two objects. If one of the cores is much denser than the other (for example, if a BH/NS merges with a giant star), a

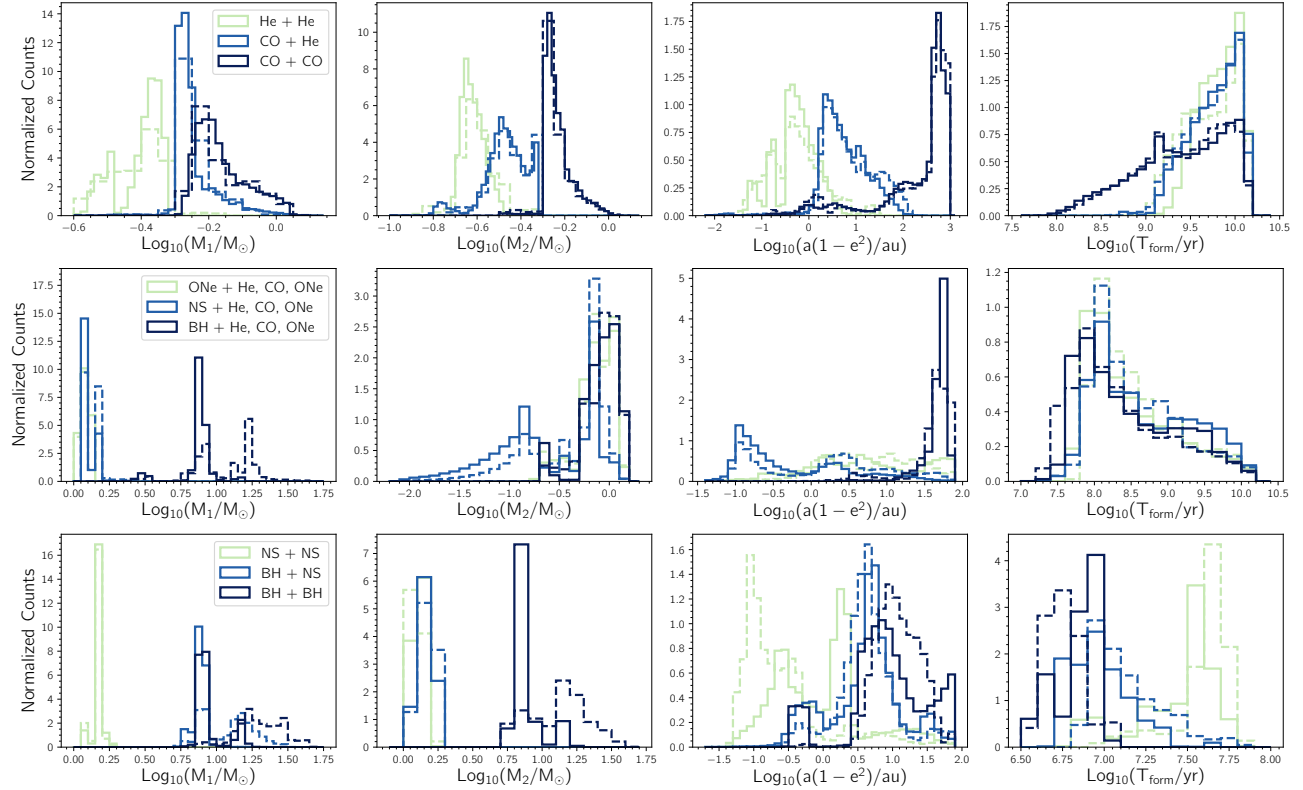


Figure 2. Normalized histograms of the primary mass, secondary mass, semilatus rectum, and time of binaries at formation with different combinations of WDs, NSs, and BHs. The WDs are split into separate populations for helium (He), carbon/oxygen (CO), and oxygen/neon (ONe) sources. The solid lines show the formation properties of the solar metallicity population while the dashed lines show the 15% solar metallicity population.

common envelope-like event ensues. However, if the two stars have comparable compactness (for example, in the case of a roughly equal-mass MS–MS merger), then the merger may result in efficient mixing of the two objects. In either case, the stellar age of the merger product must be specified. Here we adopt the prescriptions of Hurley et al. (2002) to determine outcomes of stellar mergers, with one exception, outlined below.

In the case of a MS–MS merger, we assume the stellar age of the MS merger product is given by

$$t_3 = f_{\text{rejuv}} \frac{t_{\text{MS3}}}{M_3} \left(\frac{M_1 t_1}{t_{\text{MS1}}} + \frac{M_2 t_2}{t_{\text{MS2}}} \right) \quad (8)$$

where M_1 and M_2 are the masses of the two merger components, $M_3 = M_1 + M_2$ is the mass of the merger product (assuming the stars merge without mass loss; Hurley et al. 2002), t_{MS1} , t_{MS2} , and t_{MS3} are the MS lifetimes of the two merger components and the merger product, respectively, and t_1 and t_2 are the stellar ages of the two merger components at the time of merger. f_{rejuv} is a factor which determines the amount of rejuvenation the merger product experiences through mixing. This factor of course depends upon the internal structure of

the two stars as well as the nature of the merger (i.e., the relative velocity of the two objects at coalescence). In original BSE, a fixed value of 0.1 is assumed for f_{rejuv} . However, in many instances this likely leads to over-rejuvenation of the merger product. Here we include f_{rejuv} as a free parameter, and adopt $f_{\text{rejuv}} = 1$ as our default value.

The outcome of stellar mergers and collisions is expected to play a critical role in dense star clusters where dynamical interactions lead to a pronounced increase in stellar mergers/collisions relative to isolated binaries (e.g., Hills & Day 1976; Bacon et al. 1996; Lombardi et al. 2002; Fregeau & Rasio 2007; Leigh et al. 2011). The details of these merger products have important implications for blue straggler stars (e.g., Sandage 1953; Chatterjee et al. 2013) as well as the formation of massive BHs (e.g., Portegies Zwart & McMillan 2002; Gürkan et al. 2004; Kremer et al. 2019a). Thus when modeling stellar and binary evolution in collisional environments like globular clusters, care must be taken when assigning the ages of stars upon collision/merger. We adopt the merger products from the collision matrix Hurley et al. (2002) (Table 2), but caution that the un-

modified version of BSE contains a typo which causes the merger of two He-MS stars to produce a MS star.

4. THE MILKY WAY POPULATION OF COMPACT BINARIES

As an illustration of the capabilities of COSMIC, we simulate the Milky Way population of binaries containing combinations of white dwarfs (WDs), neutron stars (NSs), and black holes (BHs) with orbital periods $10\text{ s} < P_{\text{orb}} < 10^5\text{ s}$. Several population synthesis investigations using different stellar evolution codes (e.g., Hils et al. 1990; Nelemans et al. 2001; Nelemans et al. 2001; Ruiter et al. 2010; Nissanke et al. 2012; Yu & Jeffery 2013; Liu & Zhang 2014; Korol et al. 2017; Lamberts et al. 2018, 2019) have considered how Galactic compact binary populations are affected by different treatments of the binary evolution physics (e.g., common envelope evolution, metallicity-dependent stellar winds, etc.), different initial conditions (e.g., stellar IMF, and initial distributions of binary separation and eccentricity), and different assumptions for the Galactic SFH. As a fiducial binary evolution model, we implement several of the updated prescriptions described in section 3 to be consistent with the models used in Kremer et al. (2019b). In particular, we assume that compact objects are formed with the ‘rapid’ model from Fryer et al. (2012) and that BH natal kicks are fallback modulated. We assume that ECSNe follow the Podsiadlowski et al. (2004) prescriptions and do not apply any ultra-stripped SNe prescriptions. Unless otherwise noted, we implement the defaults in the original BSE code release.

As described in section 2, we simulate a population for each of the Milky Way mass components: the thin and thick disks and the bulge. For the thin disk and the bulge we generate a fixed population of solar metallicity binaries from a single burst of star formation which evolves for 13.7 Gyr. Similarly, we generate a fixed population of binaries with 15% solar metallicity from a single burst of star formation which evolves for 13.7 Gyr. We apply an upper orbital period cut of $1000 R_{\odot}$ for systems with a WD or NS primary component since their GW merger time exceeds a Hubble time by several orders of magnitude. The number of binaries simulated in each population for both metallicities, as well as the total mass of all stars formed (including single stars) in the population are detailed in Table 1.

Figure 2 shows the distributions of the masses, semi-latera recta, and times of several combinations of WD, NS, and BH binaries at compact object formation. The solar metallicity (solid lines) populations follow similar trends when compared to the 15% solar metallicity population, with the exception of the BH populations.

Table 1. Summary of the fixed population statistics; WD denotes the population containing He, CO, and ONe WDs.

Population	Z [Z_{\odot}]	N _{simulated}	M _{stars} [M_{\odot}]
He + He	0.02	213418	2.233×10^8
CO + He	0.02	134978	1.739×10^8
CO + CO	0.02	328561	1.707×10^8
ONe + WD	0.02	50892	4.452×10^8
NS + WD	0.02	267659	2.063×10^{10}
BH + WD	0.02	203149	1.244×10^{10}
NS + NS	0.02	37035	1.112×10^{10}
BH + NS	0.02	95851	2.238×10^{10}
BH + BH	0.02	366970	2.257×10^{10}
He + He	0.003	246623	1.183×10^8
CO + He	0.003	186485	1.565×10^8
CO + CO	0.003	407219	1.758×10^8
ONe + WD	0.003	68051	4.694×10^8
NS + WD	0.003	273118	2.471×10^{10}
BH + WD	0.003	206400	1.024×10^{10}
NS + NS	0.003	44813	1.541×10^{10}
BH + NS	0.003	154802	1.071×10^{10}
BH + BH	0.003	546346	1.366×10^{10}

This is primarily due to our inclusion of metallicity-dependent stellar winds, which allow for higher mass BHs. Similar to single-star evolution, the formation times of populations with a WD component are longer than those containing NS or BH components due to decreasing main sequence lifetimes with increasing progenitor mass.

4.1. Calculation of Signal-to-Noise Ratio

The characteristic strain of a GW source, as well as the signal-to-noise ratio (S/N) for a given GW detector, can be calculated in several different approximations, depending upon the properties of the source of interest. Specifically, the most general case of an sky and polarization averaged eccentric and chirping source can be approximated if the source is circular and/or stationary (non-chirping). In this section, we describe the computation of the characteristic strain and LISA S/N in four different regimes: eccentric and chirping, circular and chirping, eccentric and stationary, and circular and stationary.

In the most general case of an eccentric chirping source, the characteristic strain at the n^{th} harmonic can be written as (e.g., Barack & Cutler 2004):

$$h_{c,n}^2 = \frac{1}{(\pi D_L)^2} \left(\frac{2G}{c^3} \frac{\dot{E}_n}{f_n} \right). \quad (9)$$

Here, D_L is the luminosity distance to the source and f_n is the source-frame GW frequency of the n^{th} harmonic given by $f_n = n f_{\text{orb}}$ where f_{orb} is the source-frame orbital frequency. f_n is related to the observed (detector frame) GW frequency, $f_{n,d}$, by $f_n = f_{n,d}(1+z)$.

\dot{E}_n is the time derivative of the energy radiated in GWs at source-frame frequency, f_n , which to lowest order is given by (e.g., Peters & Mathews 1963):

$$\dot{E}_n = \frac{32}{5} \frac{G^{7/3}}{c^5} \left(2\pi f_{\text{orb}} \mathcal{M}_c\right)^{10/3} g(n, e) \quad (10)$$

where \mathcal{M}_c is the source-frame chirp mass, which is related to detector-frame chirp mass, $\mathcal{M}_{c,d}$ by

$$\mathcal{M}_c = \frac{\mathcal{M}_{c,d}}{1+z} = \frac{(M_1 M_2)^{3/5}}{(M_1 + M_2)^{1/5}} \frac{1}{1+z}. \quad (11)$$

$\dot{f}_n = n \dot{f}_{\text{orb}}$ is given by:

$$\dot{f}_n = n \frac{96}{10\pi} \frac{(G\mathcal{M}_c)^{5/3}}{c^5} \left(2\pi f_{\text{orb}}\right)^{11/3} F(e) \quad (12)$$

where $F(e) = [1 + (73/24)e^2 + (37/96)e^4]/(1 - e^2)^{7/2}$. Combining Equations 9, 10, and 12 we obtain the characteristic strain in the detector frame:

$$h_{c,n,d}^2 = \frac{2}{3\pi^{4/3}} \frac{(G\mathcal{M}_c)^{5/3}}{c^3 D_L^2} \frac{1}{f_{n,d}^{1/3} (1+z)^2} \left(\frac{2}{n}\right)^{2/3} \frac{g(n, e)}{F(e)} \quad (13)$$

For $z \approx 0$, the distinction between the detector-frame and source-frame quantities becomes negligible. In this case, $h_{c,n,d} \approx h_{c,n}$, $f_{n,d} \approx f_n$, and $\mathcal{M}_{c,d} \approx \mathcal{M}_c$, allowing us to write Equation 13 as:

$$h_{c,n}^2 = \frac{2}{3\pi^{4/3}} \frac{(G\mathcal{M}_c)^{5/3}}{c^3 D_L^2} \frac{1}{f_n^{1/3}} \left(\frac{2}{n}\right)^{2/3} \frac{g(n, e)}{F(e)}. \quad (14)$$

Henceforth, we ignore dependence on redshift for simplicity, an appropriate approximation since $z \ll 1$ for the Galactic sources of interest in this analysis. For binaries with $e = 0$, all GW power is emitted in the $n = 2$ harmonic. Thus, the characteristic strain for circular and chirping binaries is

$$h_{c,2}^2 = \frac{2}{3\pi^{4/3}} \frac{(G\mathcal{M}_c)^{5/3}}{c^3 D_L^2} \frac{1}{f_2^{1/3}}, \quad (15)$$

where we have simply taken $n = 2$ in Equation 14.

For eccentric and stationary sources where $\dot{f} < f/T_{\text{obs}}$, the GW strain of the n^{th} harmonic is given by:

$$h_n^2 = \frac{64}{5} \frac{(G\mathcal{M}_c)^{10/3}}{c^8} \frac{(\pi f_n)^{4/3}}{D_L^2} g(n, e). \quad (16)$$

Table 2. Summary of the Milky Way population statistics; WD denotes the population containing He, CO, and ONe WDs.

Component	Population	N_{total}	$S/N > 7$
Thin Disk	He + He	4.13×10^7	18300
	CO + He	3.35×10^7	330
	CO + CO	8.32×10^8	2900
	ONe + WD	1.99×10^7	460
	NS + WD	5.62×10^6	700
	BH + WD	1.74×10^6	0
	NS + NS	3.17×10^5	10
	BH + NS	6.01×10^5	120
	BH + BH	1.52×10^6	16
Thick Disk	He + He	3.01×10^7	11800
	CO + He	1.72×10^7	20
	CO + CO	3.33×10^7	130
	ONe + WD	1.81×10^6	30
	NS + WD	2.56×10^7	70
	BH + WD	1.14×10^7	0
	NS + NS	1.65×10^6	1
	BH + NS	1.12×10^7	7
	BH + BH	4.70×10^7	9
Bulge	He + He	8.51×10^6	5000
	CO + He	6.91×10^6	20
	CO + CO	1.71×10^7	100
	ONe + WD	4.10×10^6	14
	NS + WD	1.16×10^6	20
	BH + WD	3.59×10^5	0
	NS + NS	6.5×10^4	0
	BH + NS	1.24×10^5	3
	BH + BH	3.13×10^5	0
		Total	4.06×10^8 4.01×10^4

Here we have divided Equation 15 by the number of cycles, N , observed for a source within a given frequency bin: $N = f^2/\dot{f}$ (see, e.g., Moore et al. 2015). The strain for a stationary and circular source is obtained from Equation 16 and adopting $n = 2$.

Having written the expressions for characteristic strain in the four different circular/eccentric, stationary/chirping regimes, we now go on to show how to calculate the LISA S/N . For chirping and eccentric sources, S/N is computed as

$$\left(\frac{S}{N}\right)^2 = \sum_{n=1}^{\infty} \int_{f_{\text{start}}}^{f_{\text{end}}} \left[\frac{h_{c,n}(f_n)}{h_f(f_n)} \right]^2 d \ln f_n, \quad (17)$$

where $h_{c,n}$ is given by Equation 9, and h_f is the characteristic LISA noise curve, which we take from (Robson et al. 2019). $f_{\text{start}} = n f_{\text{orb}}$ is the GW frequency emitted at the n^{th} harmonic at the start of the LISA observation

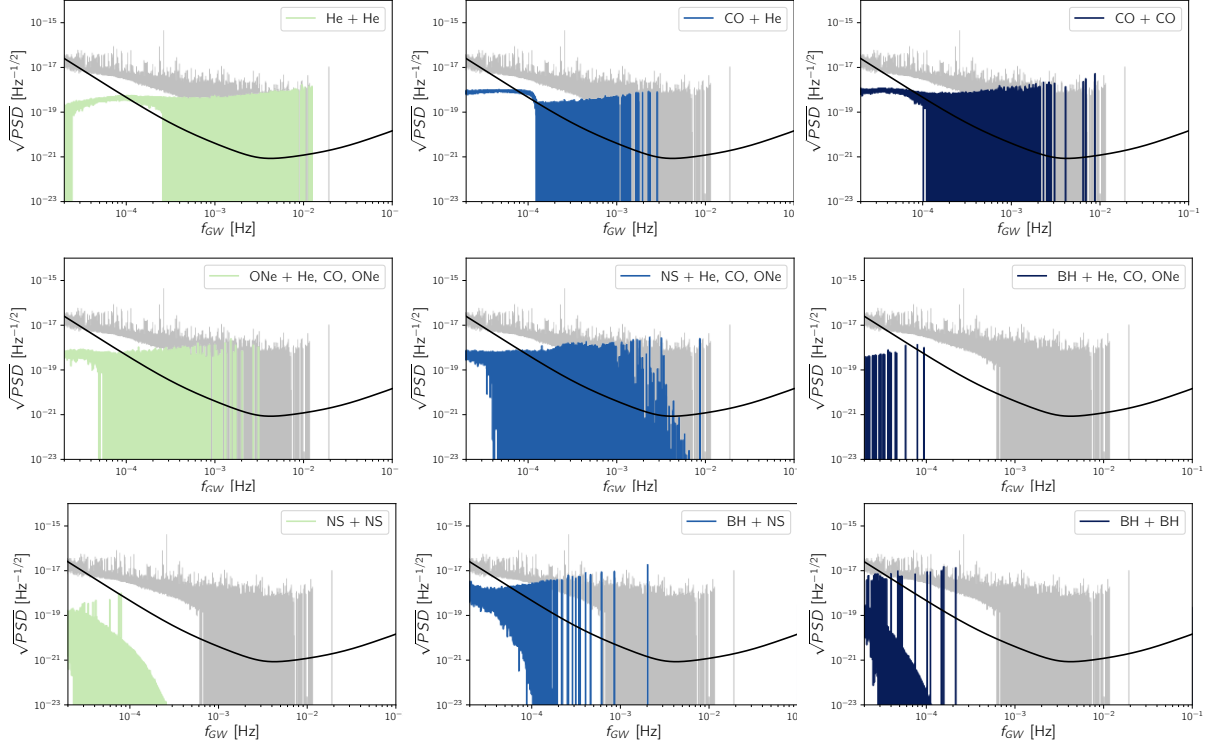


Figure 3. Root power spectral density (rPSD) as a function of frequency for each population in our Milky Way realization. The grey lines are the same in each plot and show the total rPSD from the full population.

and f_{end} is either the GW frequency at merger or the GW frequency of the n^{th} harmonic of the orbital frequency of the binary at the end of the *LISA* observation time. The characteristic noise can be expressed as

$$h_f(f_n) = \sqrt{\frac{f_n P_n(f_n)}{\mathcal{R}(f_n)}} \quad (18)$$

where $P_n(f_n)$ is the noise power spectral density of the detector and $\mathcal{R}(f_n)$ is the frequency-dependent signal response function.

For chirping circular source, $h_{c,n}$ in Equation 17 is replaced by $h_{c,2}$ (Equation 15) so that the S/N is given by

$$\left(\frac{S}{N}\right)^2 = \sum_{n=1}^{\infty} \int_{f_{\text{start}}}^{f_{\text{end}}} \left[\frac{h_{c,2}(f_n)}{h_f(f_n)} \right]^2 d \ln f_n. \quad (19)$$

For stationary sources, it is no longer necessary to integrate over frequency space. In the stationary and eccentric regime, we obtain:

$$\left(\frac{S}{N}\right)^2 \approx \sum_{n=1}^{\infty} \left[\frac{h_n(f_n)}{h_f(f_n)} \right]^2 f_n T_{\text{obs}}. \quad (20)$$

Finally, for stationary and circular sources:

$$\left(\frac{S}{N}\right)^2 \approx \left[\frac{h_2(f)}{h_f(f)} \right]^2 f T_{\text{obs}}. \quad (21)$$

In the equations above, T_{obs} is the *LISA* observation time which we take to be 4 yr. In practice the vast majority of sources are stationary or can be approximated as stationary since their evolution over the observation time spans less than 500 *LISA* bins. Based on a 4 yr observation time, this amounts to a frequency change of $\Delta f_{\text{GW}} \lesssim 5 \times 10^{-6}$ Hz and thus has a negligible effect on S/N . In the following section, we assume all sources are stationary.

4.2. The Galactic population of close WD, NS, and BH binaries

We convolve the fixed population with the SFHs and spatial distributions described in section 2 to produce a population of WD, NS, and BH binaries born in the Galaxy. Based on their birth time, and the age of each Galactic component, we evolve each binary up to the present and remove all systems that either merge, or fill their Roche Lobes. Although accreting systems may also be resolvable GW sources, and indeed may present rich opportunities for studying various aspects of binary

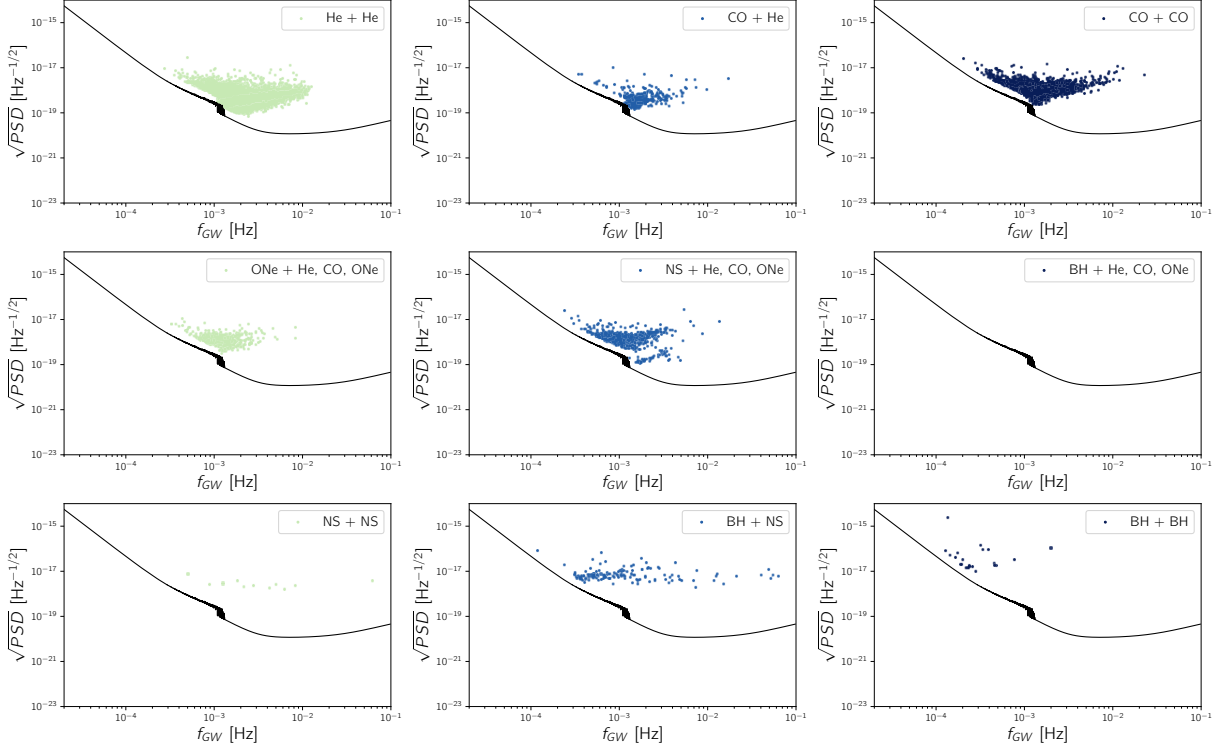


Figure 4. Scatter points of the rPSD vs GW frequency of the systems resolved with $S/N > 7$ for each population in our Milky Way realization. The simulated irreducible foreground and LISA sensitivity is shown in black.

evolution (e.g., Kremer et al. 2017; Breivik et al. 2018), we limit this study to only detached sources for simplicity. Table 2 shows a summary of the number of sources per population and Milky Way component, as well as the number of systems for which the signal to noise ratio is: $S/N > 7$ from a Milky Way population realization. Our approach for selecting resolved sources is more simple than the approach used in Korol et al. (2017) and Lamberts et al. (2019). Instead, we apply a running median with a window of 5 frequency bins to the total root power spectral density shown in Figure 3 following Benacquista & Holley-Bockelmann (2006). This produces a synthetic foreground signal similar to that shown in Korol et al. (2017). This foreground is added to the LISA power spectral density curve of Robson et al. (2019) and used to compute the signal to noise ratio as described in subsection 4.1.

The root power spectral density (rPSD), or amplitude spectral density, of each population in our Milky Way realization, along with the LISA sensitivity curve, is plotted in Figure 3. The vast majority of the signal in the rPSD is due to the population of DWDs. The characteristic shape, especially the fall off near 1 mHz, is due to the number of systems radiating GWs in a given frequency bin. At low frequencies the number of sources per bin is high both because most sources preferentially

have longer orbital periods and because the number of bins is low when compared with the number of bins at higher frequencies. As a result, at frequencies in excess of 1 mHz, there is a higher likelihood that a source occupies a unique frequency bin.

The features present in the rPSD are often smoothed out to produce a foreground (e.g., Littenberg et al. 2013; Korol et al. 2017; Lamberts et al. 2019). Here, we present the unsmoothed rPSD in order to illustrate contribution of each population to the signal. The trends of stronger signals toward higher frequency seen in the DWD population is a direct consequence of the GW signal's dependence on frequency. The decreasing GW signal with frequency in the populations containing a NS or BH is due to eccentric sources which emit GWs at harmonics of the orbital frequency.

We note that different binary evolution models will produce different rPSDs and thus different irreducible foregrounds. This may provide an avenue to distinguish different binary evolution models. In order to properly determine how well LISA can constrain binary evolution models, the variance in rPSDs produced from multiple realizations of the same model should be explored to confirm which features are present in spite of the variance. We leave this topic for a future study.

Figure 4 shows the systems resolved with $S/N > 7$ above the irreducible foreground created from the running median of the rPSD of the full population. The total number in each Galactic component is listed in Table 2. We find that the vast majority of the population of resolved compact binaries is comprised of DWD systems. Our findings are broadly consistent with most previous work (e.g. Hils et al. 1990; Nelemans et al. 2001; Ruiter et al. 2010; Yu & Jeffery 2013; Liu & Zhang 2014; Korol et al. 2017; Lamberts et al. 2018, 2019). The main differences in our predicted catalogs and previous works arise from differences in both binary evolution models as well as Galactic component masses and spatial distributions.

Similar to Lamberts et al. (2018), we find that there is a dearth of resolved BH + BH binaries even though there are $> 10^7$ of them in our total simulated population. This is also true for BH + NS binaries. In general the high number BH binaries is due to our metallicity-dependent wind prescriptions which produce higher mass compact object progenitors at low metallicities. These higher mass progenitors evolve into BHs formed with a significant amount of fallback, and thus reduced natal kicks which are less likely to unbind the binary. However, they are largely unresolved because they tend to occupy frequencies below 1 mHz. Even though the population is dominated by eccentric sources, their GW emission at harmonics above the orbital frequency does not fall above the combined rPSD of *LISA* and the foreground. We also find a much lower rate of NS + NS binaries detected by *LISA* than both Lau et al. (2019) and Andrews et al. (2019). The assumptions for both of these models are different from our model. In particular, Lau et al. (2019) assumes the initial distribution of semilatus rectum is limited to 1000 au while we place an upper limit of 1000 au. They also use the Fryer et al. (2012) delayed model, instead of the rapid model for compact object formation. Andrews et al. (2019) links the NS + NS population resolved by *LISA* directly to the observed NS + NS merger rates derived from radio observations or *LIGO/Virgo*. Since this study is simply a proof of concept for the capabilities of COSMIC,

which does not carefully include *LISA* data analysis, a detailed study of the resolved sources, and their parameter estimation is past the scope of this work.

5. DISCUSSION

We have presented a new, openly developed BPS code, COSMIC, which is based on BSE (Hurley et al. 2000, 2002). We have detailed the process COSMIC uses to produce binary populations as well as how to scale these populations to astrophysical realizations by convolving with spatial distributions and a SFH. As an illustrative example, we have simulated a Milky Way realization of the thin disk, thick disk, and bulge for all combinations of stellar-remnant binaries potentially observable by *LISA*. We find $\sim 10^8$ stellar remnant binaries exist in the Galaxy today with $\sim 10^4$ expected to be observed by *LISA* after a 4 yr observation time, with $S/N > 7$.

Future studies using COSMIC to self-consistently explore the resolved populations of several binary evolution models as well as Galactic component formation histories and spatial distribution. These studies will provide important insights into the populations containing NSs and BHs, which will also be important in comparing to current and future *LIGO/Virgo* results. Furthermore, as future electromagnetic observations produce new compact-binary catalogs, the binary evolution models can be adapted to best represent the compact binary population of the Milky Way.

ACKNOWLEDGEMENTS

The majority of our analysis was performed using the computational resources of the Quest high performance computing facility at Northwestern University which is jointly supported by the Office of the Provost, the Office for Research, and Northwestern University Information Technology. K.B. is grateful to Sylvia Toonen, Valeriya Korol, and Stephan Justham for helpful conversations about population synthesis and acknowledges support from the Jeffery L. Bishop Fellowship. J.J.A. acknowledges support by the Danish National Research Foundation (DNRF132). F.A.R. acknowledges support from NSF Grant AST-1716762 at Northwestern University.

REFERENCES

Abbott, B. P., Abbott, R., Abbott, T. D., & et al. 2018, arXiv e-prints, arXiv:1811.12907

Abbott, B. P., Abbott, R., Abbott, T. D., et al. 2017, Physical Review Letters, 119, 161101

Andrews, J. J., Breivik, K., Pankow, C., D’Orazio, D. J., & Safarzadeh, M. 2019, arXiv e-prints, arXiv:1910.13436

Andrews, J. J., Farr, W. M., Kalogera, V., & Willems, B. 2015, ApJ, 801, 32

Andrews, J. J., Zezas, A., & Fragos, T. 2018, ApJS, 237, 1

Astropy Collaboration, Robitaille, T. P., Tollerud, E. J., et al. 2013, A&A, 558, A33

Bacon, D., Sigurdsson, S., & Davies, M. B. 1996, MNRAS, 281, 830

Barack, L., & Cutler, C. 2004, *PhRvD*, 69, 082005

Barrett, J. W., Gaebel, S. M., Neijssel, C. J., et al. 2018, *MNRAS*, 477, 4685

Barrett, J. W., Mandel, I., Neijssel, C. J., Stevenson, S., & Vigna-Gómez, A. 2017, in *IAU Symposium*, Vol. 325, *Astroinformatics*, ed. M. Brescia, S. G. Djorgovski, E. D. Feigelson, G. Longo, & S. Cauvot, 46–50

Belczynski, K., Bulik, T., Fryer, C. L., et al. 2010, *ApJ*, 714, 1217

Belczynski, K., Kalogera, V., & Bulik, T. 2002, *ApJ*, 572, 407

Belczynski, K., Kalogera, V., Rasio, F. A., et al. 2008, *ApJS*, 174, 223

Belczynski, K., Heger, A., Gladysz, W., et al. 2016, *A&A*, 594, A97

Belczynski, K., Klencki, J., Fields, C. E., et al. 2017, arXiv e-prints, arXiv:1706.07053

Benacquista, M., & Holley-Bockelmann, K. 2006, *ApJ*, 645, 589

Bhattacharya, D., & van den Heuvel, E. P. J. 1991, *PhR*, 203, 1

Bondi, H., & Hoyle, F. 1944, *MNRAS*, 104, 273

Breivik, K., Kremer, K., Bueno, M., et al. 2018, *ApJL*, 854, L1

Breivik, K., Coughlin, S. C., Zevin, M., et al. 2019, COSMIC, vv3.1.0, Zenodo, doi:10.5281/zenodo.3482915. <https://doi.org/10.5281/zenodo.3482915>

Broekgaarden, F. S., Justham, S., de Mink, S. E., et al. 2019, arXiv e-prints, arXiv:1905.00910

Camacho, J., Torres, S., García-Berro, E., et al. 2014, *A&A*, 566, A86

Chatterjee, S., Rasio, F. A., Sills, A., & Glebbeek, E. 2013, *ApJ*, 777, 106

Chen, Y., Bressan, A., Girardi, L., et al. 2015, *MNRAS*, 452, 1068

Claeys, J. S. W., Pols, O. R., Izzard, R. G., Vink, J., & Verbunt, F. W. M. 2014, *A&A*, 563, A83

De Donder, E., & Vanbeveren, D. 2004, *NewAR*, 48, 861

de Mink, S. E., & Belczynski, K. 2015, *ApJ*, 814, 58

de Mink, S. E., Pols, O. R., & Hilditch, R. W. 2007, *A&A*, 467, 1181

Dominik, M., Belczynski, K., Fryer, C., et al. 2012, *ApJ*, 759, 52

—. 2013, *ApJ*, 779, 72

Eggenberger, P., Meynet, G., Maeder, A., et al. 2008, *Ap&SS*, 316, 43

Eldridge, J. J., & Stanway, E. R. 2016, *MNRAS*, 462, 3302

Eldridge, J. J., Stanway, E. R., Xiao, L., et al. 2017, *PASA*, 34, e058

Fragos, T., Andrews, J. J., Ramirez-Ruiz, E., et al. 2019, arXiv e-prints, arXiv:1907.12573

Fregeau, J. M., & Rasio, F. A. 2007, *ApJ*, 658, 1047

Fryer, C. L., Belczynski, K., Wiktorowicz, G., et al. 2012, *ApJ*, 749, 91

Fuller, J., & Ma, L. 2019, *ApJL*, 881, L1

Geller, A. M., Leigh, N. W. C., Giersz, M., Kremer, K., & Rasio, F. A. 2019, *ApJ*, 872, 165

Giacobbo, N., & Mapelli, M. 2018, *MNRAS*, 480, 2011

Giacobbo, N., Mapelli, M., & Spera, M. 2018, *MNRAS*, 474, 2959

Goldberg, D., & Mazeh, T. 1994, *A&A*, 282, 801

Gräfener, G., & Hamann, W. R. 2008, *A&A*, 482, 945

Gürkan, M. A., Freitag, M., & Rasio, F. A. 2004, *ApJ*, 604, 632

Han, Z. 1998, *MNRAS*, 296, 1019

Heggie, D. C. 1975, *MNRAS*, 173, 729

Hills, J. G., & Day, C. A. 1976, *Astrophys. Lett.*, 17, 87

Hils, D., Bender, P. L., & Webbink, R. F. 1990, *ApJ*, 360, 75

Hobbs, G., Lorimer, D. R., Lyne, A. G., & Kramer, M. 2005, *MNRAS*, 360, 974

Hurley, J. R., Pols, O. R., & Tout, C. A. 2000, *MNRAS*, 315, 543

Hurley, J. R., Tout, C. A., & Pols, O. R. 2002, *MNRAS*, 329, 897

Ivanova, N., Belczynski, K., Kalogera, V., Rasio, F. A., & Taam, R. E. 2003, *ApJ*, 592, 475

Ivanova, N., Heinke, C. O., Rasio, F. A., Belczynski, K., & Fregeau, J. M. 2008, *MNRAS*, 386, 553

Ivanova, N., & Taam, R. E. 2004, *ApJ*, 601, 1058

Izzard, R. G., Dray, L. M., Karakas, A. I., Lugaro, M., & Tout, C. A. 2006, *A&A*, 460, 565

Izzard, R. G., Glebbeek, E., Stancliffe, R. J., & Pols, O. R. 2009, *A&A*, 508, 1359

Izzard, R. G., Tout, C. A., Karakas, A. I., & Pols, O. R. 2004, *MNRAS*, 350, 407

Kaplan, D. L., Chatterjee, S., Gaensler, B. M., & Anderson, J. 2008, *ApJ*, 677, 1201

Kiel, P. D., Hurley, J. R., Bailes, M., & Murray, J. R. 2008, *MNRAS*, 388, 393

Klencki, J., Moe, M., Gladysz, W., et al. 2018, *A&A*, 619, A77

Knuth, K. H. 2006, ArXiv Physics e-prints, physics/0605197

Korol, V., Rossi, E. M., Groot, P. J., et al. 2017, *MNRAS*, 470, 1894

Kremer, K., Breivik, K., Larson, S. L., & Kalogera, V. 2017, *ApJ*, 846, 95

Kremer, K., Ye, C., , et al. 2019a

Kremer, K., Rodriguez, C. L., Amaro-Seoane, P., et al. 2019b, *PhRvD*, 99, 063003

Kroupa, P. 2001, *MNRAS*, 322, 231

Kroupa, P., Tout, C. A., & Gilmore, G. 1993, *MNRAS*, 262, 545

Kruckow, M. U., Tauris, T. M., Langer, N., Kramer, M., & Izzard, R. G. 2018, *MNRAS*, 481, 1908

Lamberts, A., Blunt, S., Littenberg, T., et al. 2019, arXiv e-prints, arXiv:1907.00014

Lamberts, A., Garrison-Kimmel, S., Hopkins, P., et al. 2018, ArXiv e-prints, arXiv:1801.03099

Lau, M. Y. M., Mandel, I., Vigna-Gómez, A., et al. 2019, arXiv e-prints, arXiv:1910.12422

Leigh, N., Sills, A., & Knigge, C. 2011, *MNRAS*, 416, 1410

Littenberg, T. B., Larson, S. L., Nelemans, G., & Cornish, N. J. 2013, *MNRAS*, 429, 2361

Liu, J., & Zhang, Y. 2014, *PASP*, 126, 211

Lombardi, James C., J., Warren, J. S., Rasio, F. A., Sills, A., & Warren, A. R. 2002, *ApJ*, 568, 939

Manchester, R. N., Hobbs, G. B., Teoh, A., & Hobbs, M. 2005, *AJ*, 129, 1993

Mapelli, M., Colpi, M., & Zampieri, L. 2009, *MNRAS*, 395, L71

Mapelli, M., & Giacobbo, N. 2018, *MNRAS*, 479, 4391

Marchant, P., Renzo, M., Farmer, R., et al. 2019, *ApJ*, 882, 36

Mazeh, T., Goldberg, D., Duquennoy, A., & Mayor, M. 1992, *ApJ*, 401, 265

McMillan, P. J. 2011, *MNRAS*, 414, 2446

Meynet, G., & Maeder, A. 2005, *A&A*, 429, 581

Miyaji, S., Nomoto, K., Yokoi, K., & Sugimoto, D. 1980, *PASJ*, 32, 303

Moe, M., & Di Stefano, R. 2017, *ApJS*, 230, 15

Moore, C. J., Cole, R. H., & Berry, C. P. L. 2015, *Classical and Quantum Gravity*, 32, 015014

Nelemans, G., Yungelson, L. R., Portegies Zwart, S. F., & Verbunt, F. 2001, *A&A*, 365, 491

Nelemans, G., Yungelson, L. R., & Zwart, S. F. P. 2001, *A&A*, 375, 890

Nelson, C. A., & Eggleton, P. P. 2001, *ApJ*, 552, 664

Ng, C.-Y., & Romani, R. W. 2007, *ApJ*, 660, 1357

Nissanke, S., Vallisneri, M., Nelemans, G., & Prince, T. A. 2012, *ApJ*, 758, 131

Nomoto, K. 1984, *ApJ*, 277, 791

—. 1987, *ApJ*, 322, 206

Nomoto, K., & Kondo, Y. 1991, *ApJL*, 367, L19

Paxton, B., Bildsten, L., Dotter, A., et al. 2011, *ApJS*, 192, 3

Paxton, B., Cantiello, M., Arras, P., et al. 2013, *ApJS*, 208, 4

Paxton, B., Marchant, P., Schwab, J., et al. 2015, *ApJS*, 220, 15

Paxton, B., Schwab, J., Bauer, E. B., et al. 2018, *ApJS*, 234, 34

Paxton, B., Smolec, R., Schwab, J., et al. 2019, *ApJS*, 243, 10

Peters, P. C., & Mathews, J. 1963, *Physical Review*, 131, 435

Podsiadlowski, P., Langer, N., Poelarends, A. J. T., et al. 2004, *ApJ*, 612, 1044

Pols, O. R., Schröder, K.-P., Hurley, J. R., Tout, C. A., & Eggleton, P. P. 1998, *MNRAS*, 298, 525

Pols, O. R., Tout, C. A., Eggleton, P. P., & Han, Z. 1995, *MNRAS*, 274, 964

Portegies Zwart, S. F., & McMillan, S. L. W. 2002, *ApJ*, 576, 899

Portegies Zwart, S. F., & Verbunt, F. 1996, *A&A*, 309, 179

Rappaport, S., Podsiadlowski, P., Joss, P. C., Di Stefano, R., & Han, Z. 1995, *MNRAS*, 273, 731

Robson, T., Cornish, N. J., & Liu, C. 2019, *Classical and Quantum Gravity*, 36, 105011

Rodriguez, C. L., Chatterjee, S., & Rasio, F. A. 2016, *PhysRevD*, 93, 084029

Ruiter, A. J., Belczynski, K., Benacquista, M., Larson, S. L., & Williams, G. 2010, *ApJ*, 717, 1006

Saio, H., & Nomoto, K. 2004, *ApJ*, 615, 444

Salpeter, E. E. 1955, *ApJ*, 121, 161

Sandage, A. R. 1953, *AJ*, 58, 61

Siess, L., Izzard, R. G., Davis, P. J., & Deschamps, R. 2013, *A&A*, 550, A100

Spera, M., & Mapelli, M. 2017, *MNRAS*, 470, 4739

Spera, M., Mapelli, M., & Bressan, A. 2015, *MNRAS*, 451, 4086

Spera, M., Mapelli, M., Giacobbo, N., et al. 2019, *MNRAS*, 485, 889

Stanway, E. R., & Eldridge, J. J. 2018, *MNRAS*, 479, 75

Stanway, E. R., Eldridge, J. J., & Becker, G. D. 2016, *MNRAS*, 456, 485

Stevenson, S., Berry, C. P. L., & Mandel, I. 2017, *MNRAS*, 471, 2801

Stevenson, S., Sampson, M., Powell, J., et al. 2019, *ApJ*, 882, 121

Tauris, T. M., Langer, N., & Kramer, M. 2012, *MNRAS*, 425, 1601

Tauris, T. M., Langer, N., Moriya, T. J., et al. 2013, *ApJL*, 778, L23

Tauris, T. M., Langer, N., & Podsiadlowski, P. 2015, *MNRAS*, 451, 2123

Taylor, S. R., & Gerosa, D. 2018, *PhRvD*, 98, 083017

Toonen, S., Claeys, J. S. W., Mennekens, N., & Ruiter, A. J. 2014, *A&A*, 562, A14

Toonen, S., & Nelemans, G. 2013, *A&A*, 557, A87

Toonen, S., Nelemans, G., & Portegies Zwart, S. 2012, *A&A*, 546, A70

van Haaften, L. M., Nelemans, G., Voss, R., et al. 2013, *A&A*, 552, A69

Vigna-Gómez, A., Neijssel, C. J., Stevenson, S., et al. 2018, *MNRAS*, 481, 4009

Vink, J. S., & de Koter, A. 2005, *A&A*, 442, 587

Vink, J. S., de Koter, A., & Lamers, H. J. G. L. M. 2001, *RMxAA*, 369, 574

Vink, J. S., Muijres, L. E., Anthonisse, B., et al. 2011, *A&A*, 531, A132

Wang, C., Lai, D., & Han, J. L. 2006, *ApJ*, 639, 1007

Webbink, R. F. 1985, *Stellar evolution and binaries*, ed. J. E. Pringle & R. A. Wade, 39

Whyte, C. A., & Eggleton, P. P. 1985, *MNRAS*, 214, 357

Woosley, S. E. 2017, *ApJ*, 836, 244

—. 2019, *ApJ*, 878, 49

Woosley, S. E., & Heger, A. 2015, in *Astrophysics and Space Science Library*, Vol. 412, *Very Massive Stars in the Local Universe*, ed. J. S. Vink, 199

Ye, C. S., Kremer, K., Chatterjee, S., Rodriguez, C. L., & Rasio, F. A. 2019, *ApJ*, 877, 122

Yu, S., & Jeffery, C. S. 2013, *Mon. Not. R. Astron. Soc.*, 429, 1602

Zevin, M., Kremer, K., Siegel, D. M., et al. 2019, *arXiv e-prints*, arXiv:1906.11299

Zorotovic, M., Schreiber, M. R., Gänsicke, B. T., & Nebot Gómez-Morán, A. 2010, *A&A*, 520, A86